ADVANCED
MATERIALS
www.advmat.d

High-Performance, Long-Life, Rechargeable Li–CO_2 Batteries based on a 3D Holey Graphene Cathode Implanted with Single Iron Atoms

*Chuangang Hu, Lele Gong, Ying Xiao, Yifei Yuan, Nicholas M. Bedford, Zhenhai Xia, Lu Ma, Tianpin Wu, Yi Lin, John W. Connell, Reza Shahbazian-Yassar, Jun Lu, Khalil Amine, and Liming Dai**

A highly efficient cathode catalyst for rechargeable Li–CO_2 batteries is successfully synthesized by implanting single iron atoms into 3D porous carbon architectures, consisting of interconnected N,S-codoped holey graphene (HG) sheets. The unique porous 3D hierarchical architecture of the catalyst with a large surface area and sufficient space within the interconnected HG framework can not only facilitate electron transport and CO_2/Li^+ diffusion, but also allow for a high uptake of Li_2CO_3 to ensure a high capacity. Consequently, the resultant rechargeable Li–CO_2 batteries exhibit a low potential gap of ≈1.17 V at 100 mA g^{-1} and can be repeatedly charged and discharged for over 200 cycles with a cut-off capacity of 1000 mAh g^{-1} at a high current density of 1 A g^{-1}. Density functional theory calculations are performed and the observed appealing catalytic performance is correlated with the hierarchical structure of the carbon catalyst. This work provides an effective approach to the development of highly efficient cathode catalysts for metal–CO_2 batteries and beyond.

The overuse of fossil fuel has caused a rapid increase in CO_2 emissions and the associated severe environmental issues, including global warming, polar ice melting, sea level rising, rain acidification, and species extinction.[1,2] As a new strategy for CO_2 sequestration and environmental remediation, the utilization of CO_2 in metal (Li)–CO_2 batteries with a high theoretical specific capacity has recently attracted considerable attention.[3,4] Apart from the CO_2 sequestration, Li–CO_2 batteries offer an advantage for energy conversion and storage, particularly for exploration of the planet Mars with an atmosphere consisting of 96% CO_2.[3]

The driving force for energy conversion and storage in Li–CO_2 batteries is the reversible redox reaction between a lithium anode and CO_2 gas cathode to form/decompose Li_2CO_3 during the discharge/charge processes. The sluggish CO_2 reduction and evolution reactions that take place at the air cathode often impede the kinetics of Li–CO_2 batteries, leading to a high voltage (>4.5 V vs Li/Li^+) for decomposing the discharge product (Li_2CO_3).[5–7] Under such a high anodic potential, the electrolyte oxidation limits the energy efficiency and cycling life of the Li–CO_2 batteries.[5–7] Therefore, efficient

---

Dr. C. Hu, Dr. Y. Xiao, Prof. L. Dai
Center of Advanced Science and Engineering for Carbon (Case4carbon)
Department of Macromolecular Science and Engineering
Case Western Reserve University
10900 Euclid Avenue, Cleveland, OH 44106, USA
E-mail: liming.dai@case.edu

Dr. C. Hu, Dr. Y. Xiao, Prof. L. Dai
The UNSW-CWRU International Joint Laboratory
School of Chemical Engineering
University of New South Wales
Sydney, NSW 2052, Australia

L. Gong, Prof. Z. Xia
Department of Materials Science and Engineering
and Department of Chemistry
University of North Texas
Denton, TX 76203, USA

Dr. Y. Yuan, Prof. R. Shahbazian-Yassar
Department of Mechanical and Industrial Engineering
University of Illinois at Chicago
Chicago, IL 60607, USA

The ORCID identification number(s) for the author(s) of this article can be found under https://doi.org/10.1002/adma.201907436.

Dr. Y. Yuan, Dr. J. Lu, Dr. K. Amine
Chemical Sciences and Engineering Division
Argonne National Laboratory
9700 South Cass Avenue, Lemont, IL 60439, USA

Dr. N. M. Bedford
Particle and Catalysis Research Group
School of Chemical Engineering
University of New South Wales
Sydney, NSW 2052, Australia

Dr. L. Ma, Dr. T. Wu
Advanced Photon Source
X-ray Science Division
Argonne National Laboratory
9700 South Cass Avenue, Lemont, IL 60439, USA

Dr. Y. Lin
National Institute of Aerospace
100 Exploration Way, Hampton, VA 23666, USA

Dr. J. W. Connell
Advanced Materials and Processing Branch
NASA Langley Research Center
Hampton, VA 23681, USA

DOI: 10.1002/adma.201907436

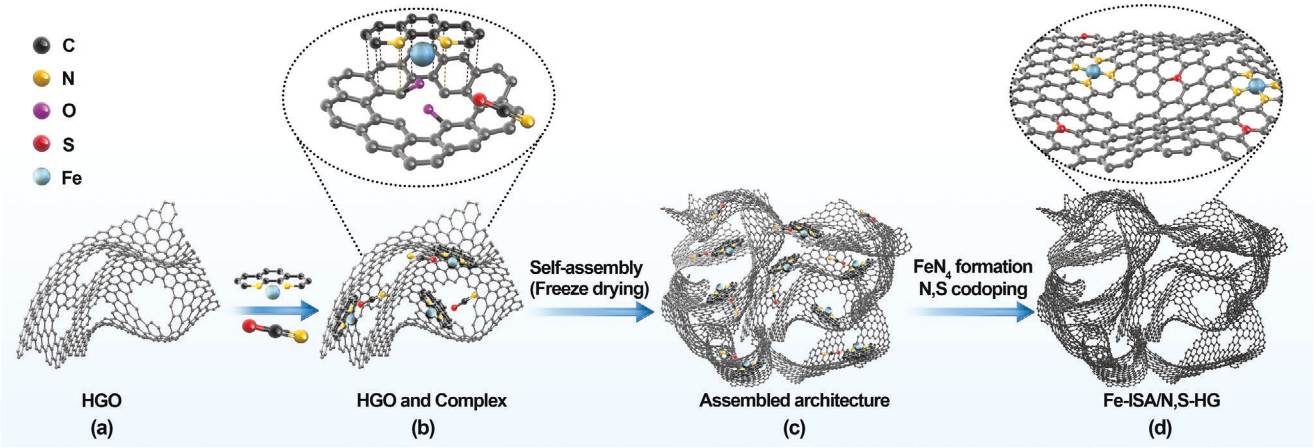

Scheme 1. Illustration of the synthesis process of Fe-ISA/N,S-HG. a) HGO. b) HGO with the complexes of phenanthroline-Fe^{3+} and thiocyanate. c) Assembled architecture of HGO with the complexes. d) The final 3D Fe-ISA/N,S-HG obtained through the Ar/NH_3 annealing and impurity removal processes.

and robust cathode catalysts are required to promote their energy efficiency and cycle life by facilitating the reversible formation and decomposition of Li_2CO_3 during the discharge/charge processes in Li–CO_2 batteries.[6,8]

Noble metal (e.g., Ir, Ru) and transition metal oxides/nitrides/carbides have been explored as bifunctional catalysts for promoting the formation and decomposition of Li_2CO_3.[5–7,9,10] Apart from their high cost, however, the use of a high content of heavy metals (ions) could not only decrease the gravimetric energy density of a battery, but also cause detrimental effects on the environmental safety and electrolyte stability.[11] Therefore, considerable effort has been devoted to the design and development of carbon-based metal-free electrocatalysts (C-MFECs) as air cathodes in Li–CO_2 batteries,[2,12–14] though their efficiency and/or stability need to be further improved. On the other hand, single-atom catalysts (SACs) have recently attracted a great deal of interest for various reactions,[15–19] including CO_2 reduction and evolution in batteries.[20] However, the easy aggregation of single atoms to form nanoparticles compromises their electrocatalytic performance. Hence, the combination of SACs and C-MFECs by anchoring single atoms onto appropriate heteroatom-doped graphene supports is emerging as a "killing two birds with one stone" strategy to overcome the aforementioned disadvantages intrinsically associated with the SACs, C-MFECs, and even noble metal catalysts.[17,19–23]

In this study, we have successfully implanted single Fe atoms into a 3D interconnected porous N,S-codoped holey graphene architecture (Fe-ISA/N,S-HG) as a highly efficient catalyst for CO_2 reduction and evolution reactions in rechargeable Li–CO_2 batteries. As pyridinic N atoms are known to preferentially locate at the edges of graphene sheets,[24] N-doped HG provides abundant pyridinic N sites for anchoring single metal atoms to form numerous "FeN_x" moieties. Our density functional theory (DFT) calculations indicated that both N,S dopants and "FeN_4" in the Fe-ISA/N,S-HG catalyst act as the active sites for CO_2 reduction and evolution reactions. Furthermore, the unique 3D hierarchical porous structure with the interconnected HG framework can facilitate the electron/ion transports while ensuring an effective exposure of the active sites (N,S dopants and "FeN_4"), leading to the formation of small Li_2CO_3 nanoparticles (<10 nm in diameter) interspersed across the HG sheets in Fe-ISA/N,S-HG after discharging. Unlike most previously reported large Li_2CO_3 nanoparticles (over 50 nm), which do not decompose readily in conventional Li–CO_2 batteries,[3,25] smaller-particle discharge products on the Fe-ISA/N,S-HG cathode should be readily decomposed upon charging. As a result, Li–CO_2 batteries based on the Fe-ISA/N,S-HG cathode exhibited a superior cell performance with a high capacity (23 174 mAh $g^{-1}_{\text{Fe-ISA/N,S-HG}}$) based on the catalyst mass, low polarization (1.17 V at 100 mA g^{-1}), good rate performance, and significantly improved long-term stability over 200 cycles even at a high current density of 1.0 A g^{-1}. To the best of our knowledge, this is the first report on the highly active bifunctional catalysts based on single atom confined in codoped carbon materials for Li–CO_2 batteries. This approach opens new avenues for the innovative design and development of novel, efficient, multifunctional hybrid catalysts for Li–CO_2 batteries and beyond.

To prepare the Fe-ISA/N,S-HG catalyst, we developed a two-step approach, involving a complexation reaction, followed by post-annealing (see, Experimental Section in the Supporting Information for details). As shown in **Scheme 1**, the π–π stacking between 1,10-phenanthroline coordinated with Fe ions and slightly oxidized HG sheets (HGO, Figure S1, Supporting Information) firmly anchored Fe single-atom species onto the Fe-ISA/N,S-HG catalyst, without any Fe agglomeration. Meanwhile, the presence of negatively charged carboxylate groups at the edge and defect sites of HGO sheets could cause the HGO sheets to repel and wrinkle, preventing the re-stacking of HGO sheets. Thus, forming a porous structure through a balanced interaction between the basal plane π–π stacking of HGO sheets and their negatively charged carboxylate edge repulsion.[26]

When the S-contained precursor (potassium thiocyanate, KSCN) was used for S heteroatom-doping in HG, we found that the primary product of iron-based nonmonoatomic impurity was an Fe-based sulfide, rather than an Fe carbide (see Figure S2, Supporting Information). Compared with the Fe carbide, the Fe-based sulfide could be much more easily removed by acid washing.[17,27] Annealing under Ar/NH_3 atmosphere

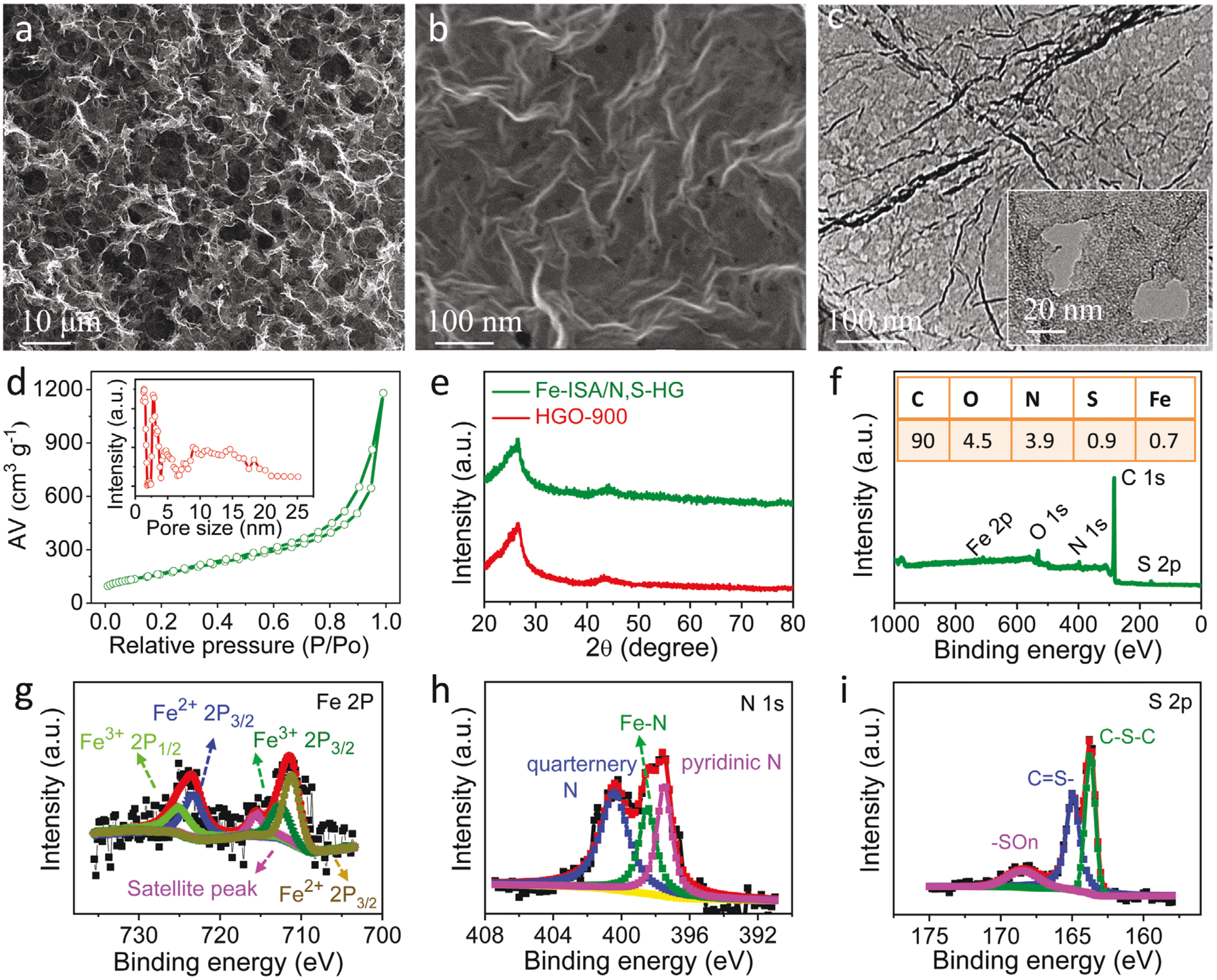

Figure 1. Structure characterization of Fe-ISA/N,S-HG. a,b) SEM images of Fe-ISA/N,S-HG under different magnifications. c) TEM along with HR-TEM (the inset) images of Fe-ISA/N,S-HG. d) Nitrogen adsorption/desorption isotherms and related pore size distribution (the insert) of Fe-ISA/N,S-HG. e) XRD patterns of Fe-ISA/N,S-HG and HG-900. f) XPS survey of Fe-ISA/N,S-HG. g–i) HR-XPS spectra of Fe 2p (g), N 1s (h), and S 2p (i), respectively.

at 900 °C, followed by acid leaching, caused sublimation of phenanthroline and complete removal of FeS$_x$, and at the same time achieving atomic dispersion of the in situ formed "Fe–N$_x$" moieties in the N,S-codoped HG network (vide infra).

Figure 1a and Figure S3 in the Supporting Information reproduce scanning electron microscopy (SEM) images from the top and side view for Fe-ISA/N,S-HG under different magnifications, which show a well-defined and interconnected 3D porous network. Compared with the transmission electron microscopy (TEM) image of the pristine HG (PHG, Experimental section and Figure S4 in the Supporting Information), pores in the surface of HG within the Fe-ISA/N,S-HG became more visible in the SEM image (Figure 1b). This is most likely due to the removal of amorphous carbon species around the pore edges by the oxidation and high-temperature annealing process during the sample preparation (Experimental Section in the Supporting Information). TEM images of the Fe-ISA/N,S-HG (Figure 1c and the insert, Figure S5, Supporting Information) further show holes of 5–20 nm in size without any metal particles, implying that Fe species, if any, have been atomically dispersed. The layer number of graphene sheets in Fe-ISA/N,S-HG was determined to be two from the randomly selected HG edges in high resolution (HR) TEM images (Figure S6, Supporting Information) with the corresponding selected area electron diffraction pattern (Figure S7, Supporting Information), which is fewer than that of PHG (five to seven layers)[28] due to the slight oxidation treatment (Experimental Section in the Supporting Information). Figure 1d and the inset show the Brunauer–Emmett–Teller isotherms and the related pore size distribution, respectively, for Fe-ISA/N,S-HG, which give a specific surface area as high as 598.0 m^2 g^{-1} with a wide range of pore size distribution over 3–20 nm, in a good consistency with the TEM observation (see Figure 1c, Figures S5 and S6, Supporting Information).

To further characterize the samples, we also performed Raman spectroscopy and X-ray diffraction (XRD) measurements. As expected, Figure S8 in the Supporting Information shows two main Raman peaks located at ≈1347.9 and 1585.0 cm^{-1}, corresponding to the D band (K-point phonons of A_{1g} symmetry) and G band (zone center phonons of E_{2g} symmetry) for defective graphitic carbon[29–31] of both HGO-900 and Fe-ISA/N,S-HG. Other Raman features include a band at ≈2690 cm^{-1} associated with 2D band corresponding to the overtone of the D band, which is symmetry-allowed and appears in the second-order Raman spectra of crystalline graphene, and a D + G combination mode (2934 cm^{-1}) induced by disorder.[32,33] Compared with HGO-900, Fe-ISA/N,S-HG showed an upshift of 2D peak and a downshift of D + G peak, indicating a more disordered structure, probably due to additional defects and/or larger holes induced by the introduction of single Fe atoms (vide supra). Similar to HGO-900, Fe-ISA/N,S-HG showed no additional diffraction peaks except the two peaks at ≈26.5° and 44.0° characteristic of the (002) and (101) plane for graphitic carbon (Figure 1e),[34] suggesting there is no crystalline Fe-based nanoparticle in the sample (vide supra).

We also performed X-ray photoelectron spectroscopy (XPS) measurements to investigate the chemical composition for Fe-ISA/N,S-HG. Figure 1f shows the XPS survey spectrum, revealing the presence of C (90.0 at%), O (4.5 at%), N (3.9 at%), S (0.9 at%), and Fe (0.7 at%). The O (4.5 at%) in Fe-ISA/N,S-HG is intrinsically associated with the reduced HG oxide and hard to be completely removed even during the thermal reduction process.[35] Although the XPS signals of Fe were very weak due to its low content, as also confirmed by the inductively coupled plasma–mass spectrometric analyses, the HR-XPS Fe 2p spectrum (Figure 1g) could be deconvoluted into five peaks at 725.2, 723.4, 715.5, 712.7, and 711.3 eV. The two peaks at 712.7 and 725.2 eV are attributable to Fe $2p_{3/2}$ and Fe $2p_{1/2}$ of Fe^{3+},[36] while another two peaks at 711.3 and 723.4 eV can be assigned to Fe^{2+}, indicating the presence of both Fe^{2+} and Fe^{3+}.[19,37,38] Figure 1h shows the HR-XPS N 1s spectrum with the characteristic peaks centered at 400.4, 398.5, and 397.1 eV attributed to quaternary N, Fe–N, and pyridinic N, respectively,[37,39] confirming the incorporation of N into the carbon skeleton and the interaction between Fe and N. The high-resolution spectrum of S 2p given in Figure 1i shows two main peaks located at 163.7 and 165.0 eV arising from C—S—C and C=S, respectively.[39,40] These results indicate the successful implantation of single iron atoms into the N,S-codoped HG within the Fe-ISA/N,S-HG sample.

Figure 2a shows a high-angle annular dark-field scanning TEM (HAADF-STEM) image for Fe-ISA/N,S-HG, which further confirms the presence of abundant holes. The corresponding element mapping images given in Figure 2b–d demonstrates the uniform distribution of N, S, and Fe in the Fe-ISA/N,S-HG sample. Figures 2e,f reproduce the atomic-resolution STEM images for Fe-ISA/N,S-HG, which clearly show homogenously dispersed bright spots of ≈0.2 nm in size arising from individual Fe single atoms, rather than nanoparticles/clusters, throughout the sample. The presence of Fe and N was also reflected by the electron energy-loss spectroscopy (EELS) measurement (Figure 2g) on the arbitrarily selected area in Figure 2f. As a limited area of about 1 to 2 Å^2 was used for the data acquisition, the EEL signals are weak, but recognizable.

To investigate Fe atoms in the Fe-ISA/N,S-HG sample at an atomic state, we further performed the X-ray absorption near edge structure (XANES) spectroscopy at the Fe K-edge. As can be seen from the XANES spectra in Figure 2h, Fe-ISA/N,S-HG shows an E_0 characteristic of Fe^{2+} with a high white line intensity, and an overall profile similar to single-atom catalysts embedded in a doped-graphene matrix.[41,42] The extended X-ray absorption fine structures (EXAFS, Figure 2i) from Fourier transform of the XAS data exhibit only one main peak at ≈1.5 Å for Fe-ISA/N,S-HG (nonphase corrected), corresponding to the first coordination shell of Fe–N. The absence of an Fe–Fe peak (around 2.2 Å) indicates that there is no metallic Fe cluster with atomically dispersed Fe atoms across the N,S-doped HG.[43] Least-square EXAFS fittings (Figure S9a–c, Supporting Information) were carried out and the obtained detailed structural parameters are listed in Table S1 in the Supporting Information. The coordination number of Fe in Fe-ISA/N,S-HG was determined to be 4.07 ± 0.32 at a bond length of 2.03 ± 0.02 Å. In addition, longer-range Fe–N coordination spheres were modeled at distances of 2.64 ± 0.05 and 2.93 ± 0.05 Å with a coordination number of 4.06 ± 0.31 and 4.12 ± 0.40, respectively. The coordination numbers and the associated distance matched very well with those of the model atomic structure shown in Figure S9d in the Supporting Information. S K-edge XANES measurement was also carried out to investigate the valance of sulfur in Fe-ISA/N,S-HG (Figure 2j), which reveals a usual valence of nearly 0 for sulfur in the Fe-ISA/N,S-HG sample.[44,45] This, together with the HR-XPS spectrum of S 2p (Figure 1i), is consistent with the presence of "—C—S—" covalent bonding in Fe-ISA/SNC since S has a very similar electronegativity (2.58) to that of C (2.55).[46]

To evaluate the electrocatalytic performance for Fe-ISA/N,S-HG, we fabricated and tested Li–CO_2 coin cells with a cathode based on the as-prepared Fe-ISA/N,S-HG, Fe-ISA/N,S-G (i.e., 3D reduced graphene oxide without holes implanted with single iron atoms, Figures S10–S12 in the Supporting Information), and HGO-900, respectively. **Figure 3**a shows the full discharge/charge profiles for a Li–CO_2 battery with the Fe-ISA/N,S-HG cathode, which exhibited a discharge capacity and charge capacity of 23 174 and 21 520 mAh $g^{-1}_{\text{Fe-ISA/N,S-HG}}$, respectively, at a current density of 100 mA g^{-1}. The corresponding areal and volumetric discharge capacities are 4.9 mAh cm^{-2} and 405.5 mAh cm^{-3}, respectively. The corresponding initial Coulombic efficiency is around 92.9%, implying the effective decomposition of Li_2CO_3 on Fe-ISA/N,S-HG during the charging process. In contrast, counterpart cathodes based on the Fe-ISA/N,S-G cathode (discharge: 15 279.9; charge: 12 007.0 mAh $g^{-1}_{\text{Fe-ISA/N,S-G}}$), and HGO-900 cathode (discharge: 12 136.8; charge: 9496.7 mAh $g^{-1}_{\text{HGO-900}}$) at the same current density exhibited much lower capacities with an initial Coulombic efficiency of ≈78.6% and 78.2%, respectively (Figure 3a). The corresponding cyclic voltammetry curves (Figure S13, Supporting Information) display a more positive shift for the onset potential of the cathodic peak and more negative shift on the anodic peak for the battery with Fe-ISA/N,S-HG compared with those of the battery with HGO-900, suggesting, once again, superb catalytic activities for Fe-ISA/N,S-HG.

For comparison, we also investigated Li–CO_2 batteries based on the traditional reduced graphene oxide (RGO, Figure S14 in the Supporting Information), N,S-codoped HG (Experimental Section, Figures S15 and S16 in the Supporting Information),

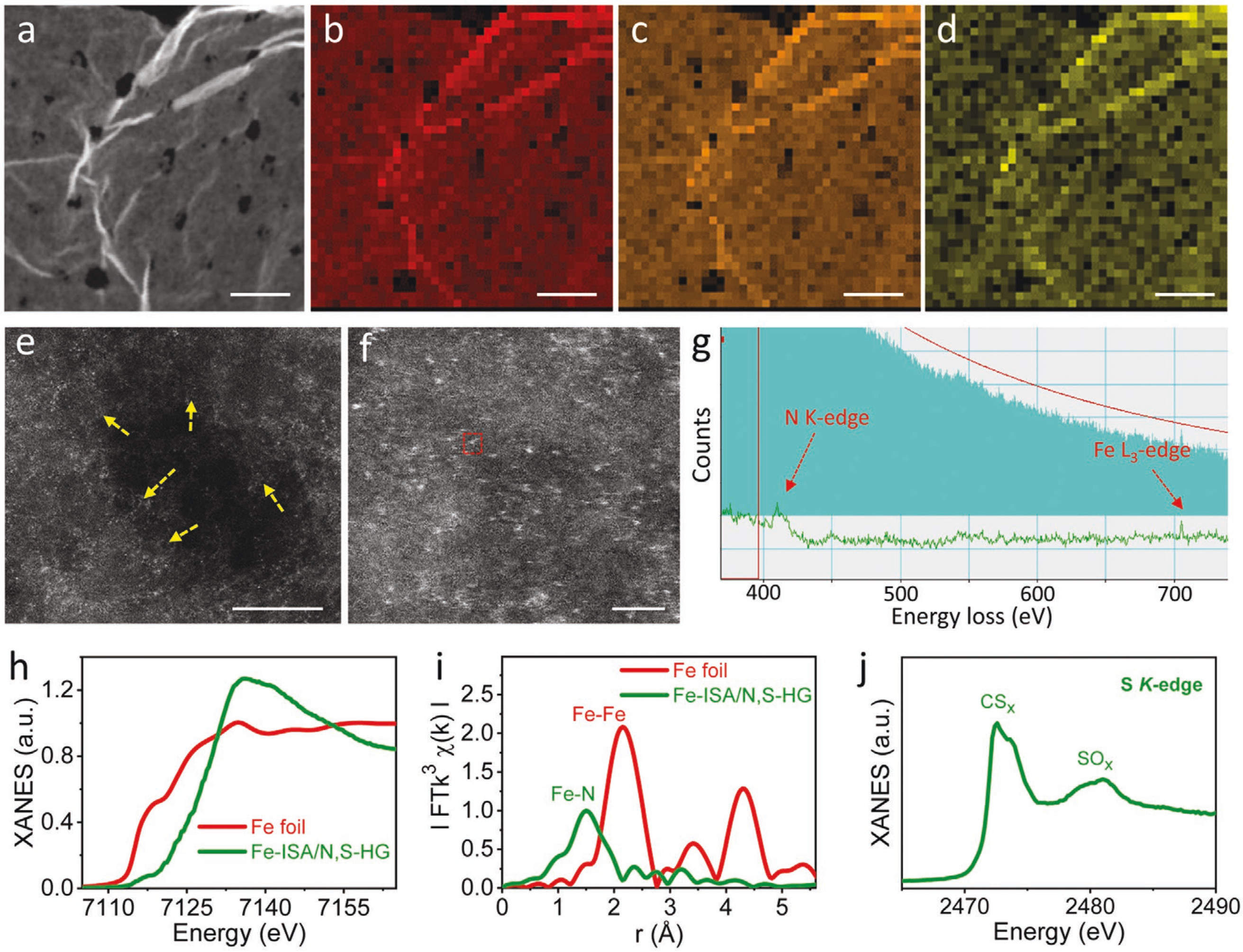

Figure 2. Structure characterization of Fe single atom in Fe-ISA/N,S-HG. a) HAADF-STEM image of Fe-ISA/N,S-HG. b–d) The corresponding energy-dispersive X-ray spectroscopy mapping images of N, S, and Fe elements of (a). e,f) Atomic-resolution STEM images of Fe-ISA/N,S-HG. g) EELS spectrum of the selected region in (f). h,i) Fe K-edge XANES and EXAFS for Fe-ISA/N,S-HG and Fe foil. j) S K-edge XANES spectra of Fe-ISA/N,S-HG. Scale bars, (a–d): 50 nm; (e): 5 nm; (f): 1 nm.

Fe/N,S-HG (obtained under the same conditions as for the Fe-ISA/N,S-HG, but without acid etching—see Experimental Section and Figure S2 in the Supporting Information) as the cathodes. Among them, the Fe-ISA/N,S-HG exhibited the smallest potential gap of ≈1.17 V with the highest discharge potential (2.78 V) and the lowest charge potential (3.95 V, Figure 3b,c, Figures S17 and S18 in the Supporting Information), and hence the highest bifunctional catalytic activity for the formation and decomposition of Li_2CO_3. Even at a current density as high as 1 A g^{-1} (Figure 3d, Figures S19 and S20 in the Supporting Information), the Fe-ISA/N,S-HG still exhibited a narrow discharge/charge potential gap of ≈1.61 V with a high retention (80.1%) after 100 cycles (cut-off capacity 1000 mAh g^{-1}), showing a superior stability to other catalysts (Fe-ISA/N,S-G and HGO-900) investigated in this study that were tested at an even lower current density of 400 mA g^{-1} (Figures S21 and S22, Supporting Information). The value of 1.17 V (at 100 mA g^{-1}) for the overpotential of Li–CO_2 batteries based on the Fe-ISA/N,S-HG cathode is much lower than those of most Li–CO_2 batteries previously reported based on carbon and even certain metal catalysts (Table S2, Supporting Information). Furthermore, Li–CO_2 batteries based on the Fe-ISA/N,S-HG cathode exhibited an excellent rate capability (Figure 3e and Figure S23 in the Supporting Information) with remarkable reversibility in the discharge potential upon reducing the current density back to 100 mA g^{-1}. Unlike the Fe-ISA/N,S-HG cathode, however, the Fe-ISA/N,S-G, Fe/N,S-HG, and HGO-900 cathodes could be cycled only up to 800–1000 mA g^{-1} with a dramatic decay in the discharge potential (Figure 3e and Figure S24 in the Supporting Information), presumably due to their deficiency of electrocatalytic activities. The Fe-ISA/N,S-HG-based battery shows an electrochemical impedance spectrum (EIS) with a higher slope at the low-frequency region than that of its counterpart based on the Fe-ISA/N,S-G cathode (Figure S25, Supporting Information), indicating that the holey structure in graphene sheets facilitated the ion diffusion to effectively reduce the ionic and Ohmic resistances.[47] Besides, these holes could not only improve the gas/electrolyte diffusion, but also provide abundant

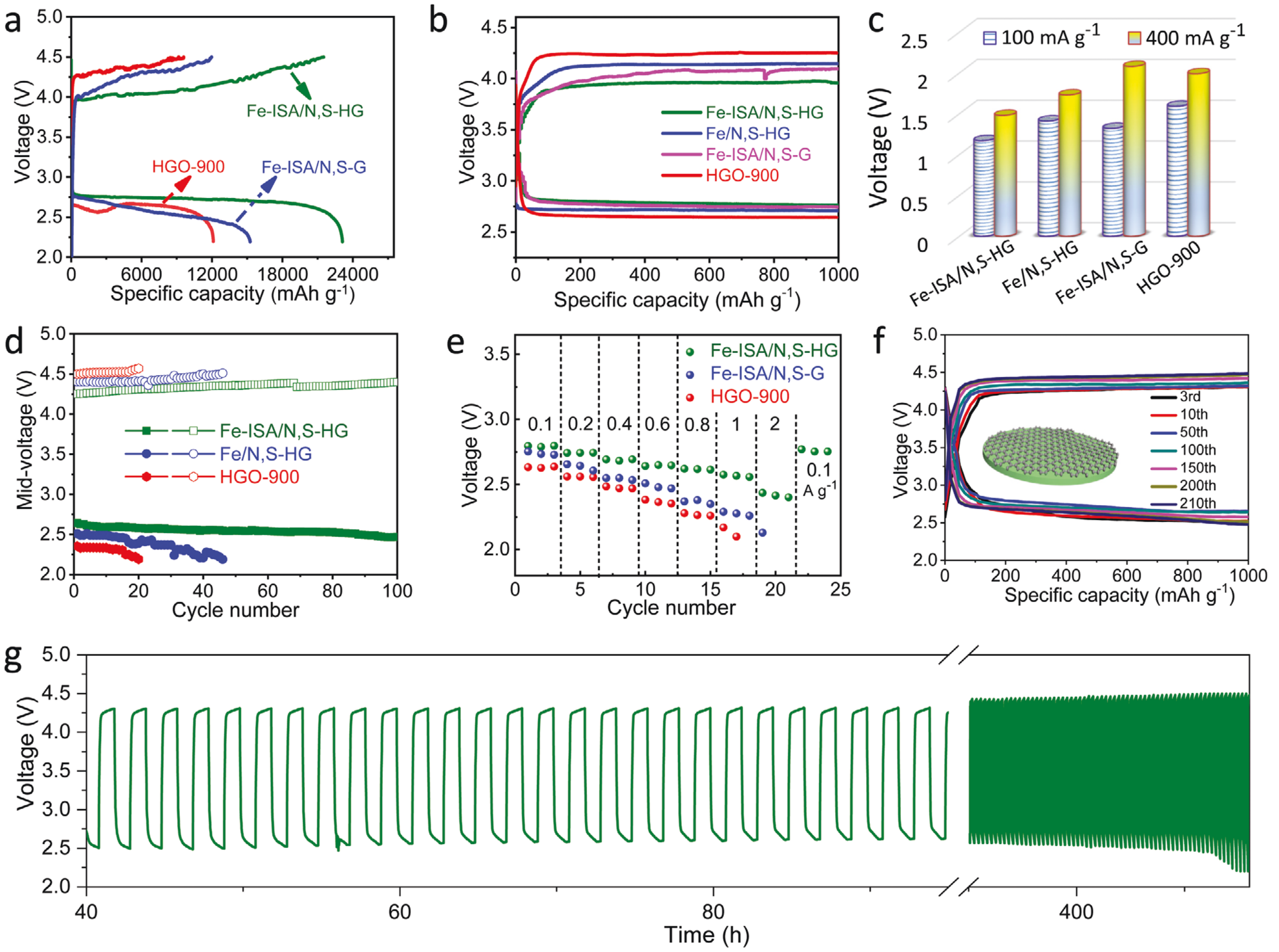

Figure 3. Electrocatalytic performance evaluation of the various cathodes in Li–CO_2 batteries. a) Full discharge/charge profiles of Fe-ISA/N,S-HG, Fe-ISA/N,S-G, and HGO-900 tested at 100 mA g^{-1}. b) Initial discharge/charge profiles of Fe-ISA/N,S-HG, Fe/N,S-HG, Fe-ISA/N,S-G, and HGO-900 at 100 mA g^{-1} under the limited discharge/charge capacities of 1000 mAh g^{-1}. c) Potential gap comparison for the Fe-ISA/N,S-HG-, Fe/N,S-HG-, Fe-ISA/N,S-G-, and HGO-900-based Li–CO_2 batteries tested at current densities of 100 and 400 mA g^{-1}, respectively. d) Cycling performance comparison of Fe-ISA/N,S-HG, Fe/N,S-HG, and Fe-ISA/N,S-G, at 1 A g^{-1}. e) Capacity comparison of Fe-ISA/N,S-HG, Fe-ISA/N,S-G, and HGO-900 at various current densities. f) Discharge/charge profiles, and g) cycling performance tested at 1 A g^{-1} of Fe-ISA/N,S-HG electrode with a Li-protected anode (Li foil coated with RGO).

catalytic active sites (N,S codoping and “Fe–N” moieties) and more available space to accommodate the discharge product. Thus, the holey structure of the graphene substrate that supports single Fe atoms plays an important role in ensuring the high performance of the Li–CO_2 batteries.

The superior catalytic activities of the Fe-ISA/N,S-HG cathode could facilitate decomposition of the Li_2CO_3 discharge product, leading to a low charge potential, a narrow overpotential gap, and good long-term stability (e.g., >100 cycles to 1000 mAh g^{-1} at 1 A g^{-1}, Figure 3d). Although it was found that CO_2 could contribute to the formation of stable solid electrolyte interface layers to some extent,[48] and that CO_2 dissolved in the dimethyl sulfoxide electrolyte could also corrode the Li anode after long-term cycling,[49] 210 cycles (Figures 3f,g and Figure S26 in the Supporting Information) were achieved for a Li–CO_2 battery based on the Fe-ISA/N,S-HG cathode with a Li anode protected by spontaneously coating with reducing graphene oxide in tetrahydrofuran for 1 h[50] (Figures S27 and S28, Supporting Information).

To gain a better understanding of the reversible CO_2 reduction and evolution on the Fe-ISA/N,S-HG cathode, we further performed XRD, Raman, and EIS measurements at the pristine/discharged/recharged states. As shown in **Figure 4**a, the pristine Fe-ISA/N,S-HG electrode before discharge showed no XRD peak above 30° of 2θ. All the peaks that appeared in the XRD profile for the discharged electrode are attributable to Li_2CO_3 while the disappearance of these peaks after the recharge process indicates good reversibility due to the efficient cathode catalyst. Similarly, the Raman peak located at ≈1087.6 cm^{-1} (Figure 4b) for the fully discharged Fe-ISA/N,S-HG cathode indicates the formation of Li_2CO_3,[14] which was largely decomposed during the subsequent recharge process, consistent with the XRD data (Figure 4a). Compared with the pristine Fe-ISA/N,S-HG electrode, the discharged electrode showed an EIS spectrum with a significantly larger semicircle (Figure 4c) due to the formation of insulating Li_2CO_3,[3] leading to an increased interfacial and charge-transfer impedance. Subsequent recharging largely recovered the EIS spectrum of the

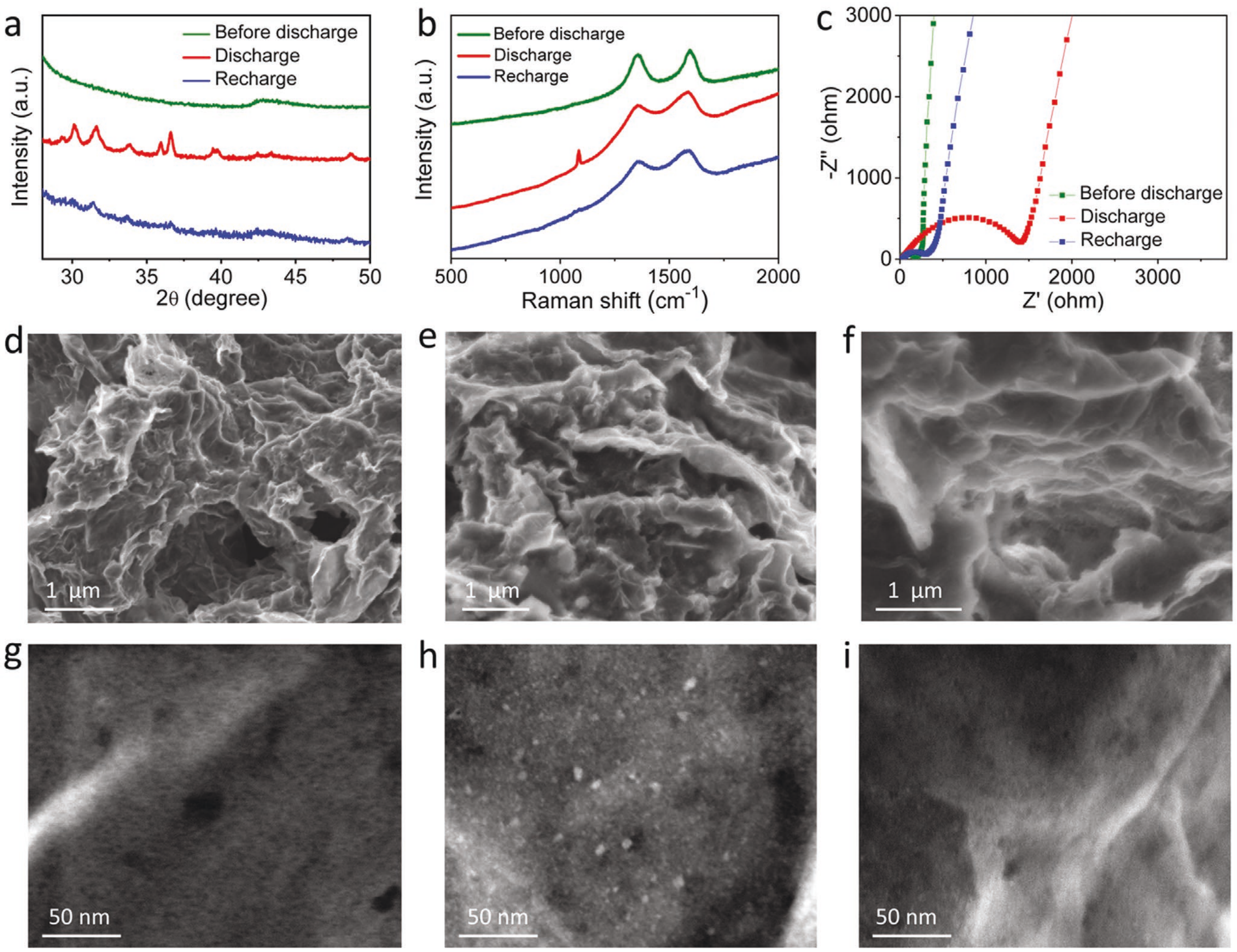

Figure 4. Reversibility of the Fe-ISA/N,S-HG cathode in Li–CO_2 batteries. a) XRD patterns, b) Raman spectra, c) EIS spectra of Li–CO_2 battery with an Fe-ISA/N,S-HG cathode under the pristine, fully discharged, and fully recharged states, respectively. d–f) SEM images and g–i) STEM images of the pristine, fully discharged, and fully recharged Fe-ISA/N,S-HG.

pristine electrode (Figure 4c), implying efficient decomposition of the discharge product during the charging process.[51] The pristine Fe-ISA/N,S-G electrode showed a similar interfacial impedance (high-frequency part), but a much larger charge-transfer impedance (high-middle-frequency part; Figure S29, Supporting Information) when compared with those of Fe-ISA/N,S-HG electrode. EIS spectrum of the Fe-ISA/N,S-G electrode without the holey structure did not return to that of the pristine electrode after recharging (Figure S29, Supporting Information), indicating, once again, the importance of the holey structure of graphene to the battery performance.

Figures 4d–f show SEM images for the Fe-ISA/N,S-HG cathode before and after the discharge/recharge processes, along with the corresponding HR-STEM images (Figures 4g–i). As can be seen, small particles with a diameter of 2–10 nm formed on the Fe-ISA/N,S-HG electrode upon discharging (Figures 4e,h and Figures S30 and S31 in the Supporting Information). Unlike those large Li_2CO_3 nanoparticles (over 50 nm) formed on the previously reported cathode materials[3,25] or the N,S-codoped HG (around 20 nm, Figure S32 in the Supporting Information), the aforementioned small particles on the Fe-ISA/N,S-HG electrode could be readily decomposed during the charging process (Figure 4f,i and Figure S33 in the Supporting Information), ensuring a low charge potential, good reversibility, and superior long-term stability. Clearly, Fe-ISA/N,S-HG exhibited an outstanding combination of the properties required for an advanced cathode material in high-performance Li–CO_2 batteries.

To obtain a clear mechanistic understanding of the high performance for the Fe-ISA/N,S-HG catalyst toward CO_2 reduction and evolution, we performed DFT calculations to simulate the electronic structures of various active sites and calculated the free energy for CO_2 adsorption.[52] **Figures 5**a–e show the model structures for N-doped graphene, S-doped graphene, N,S-codoped graphene, Fe/N-doped graphene with the "FeN_4" moieties in the center and at the edge of the graphene sheet, and the catalytically active sites were identified in this theoretical work.

Since heteroatom-doping is known to cause the redistribution of the effective charge and spin density on the carbon skeleton,[53] the active site and catalytic performance will be related to the charge density (Figures S34 and S35, Supporting

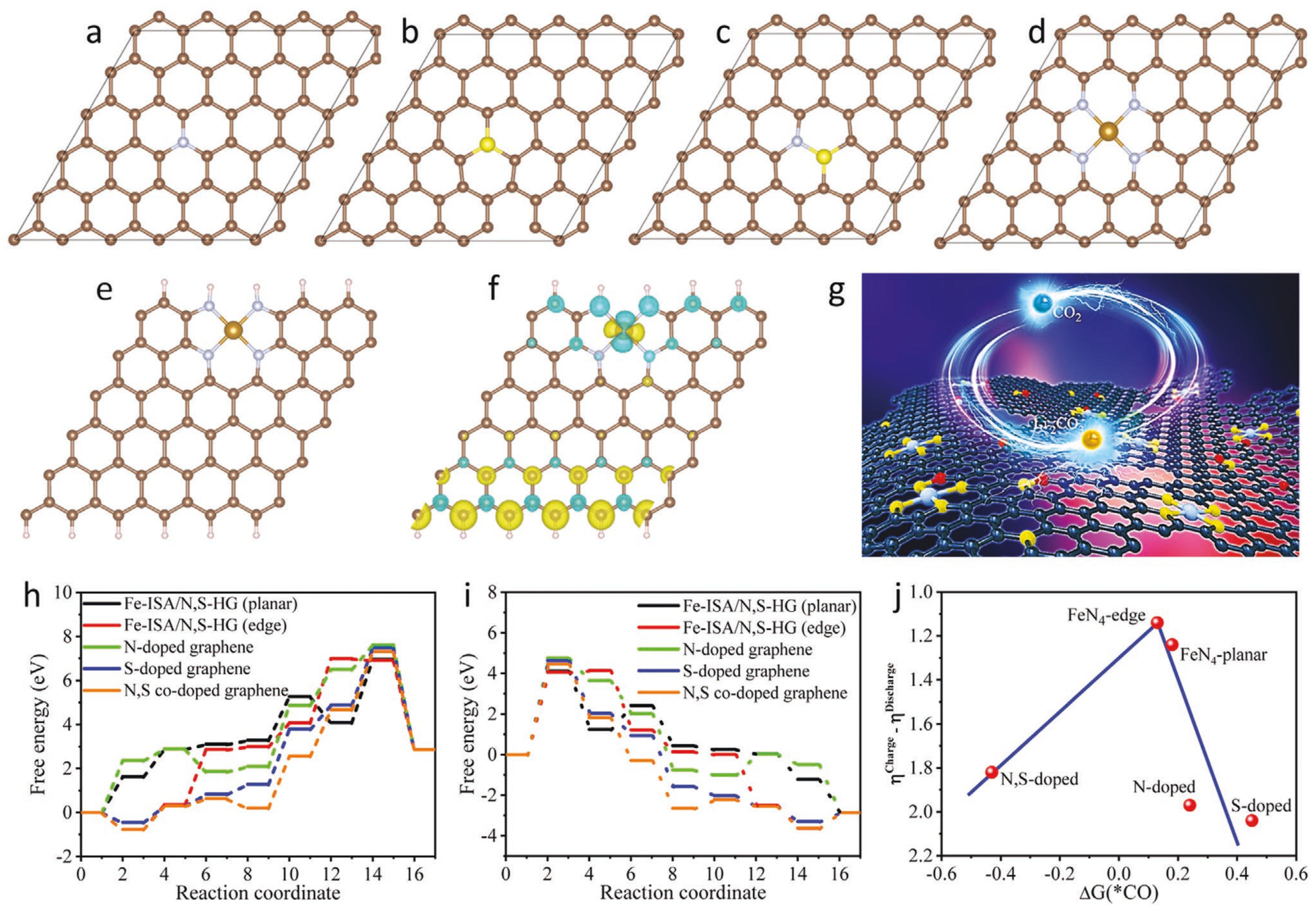

Figure 5. Mechanistic understanding of the reduction and evolution of CO_2 in the Li–CO_2 batteries during the charge and discharge. a–e) The model structures of: a) N-doped graphene, b) S-doped graphene, c) N,S-doped graphene, and d,e) Fe/N-doped graphene with the "FeN_4" moieties in the center (d) and at the edge (e) of the graphene. The brown, silver, yellow, and gold balls represent C, N, S, and Fe, respectively. f) Spin density distribution of edged "FeN_4" moiety in the carbon skeleton. g) Schematic diagram of the formation and decomposition of Li_2CO_3 on the catalyst surface (Fe-ISA/N,S-HG). h,i) Schematic Gibbs free energy diagrams of formation and decomposition of the Li_2CO_3 during discharging (h) and charging (i) processes on N,S-codoped graphene, N-doped graphene, S-doped graphene, and "FeN_4" moieties. j) The adsorption energy of *CO (ΔG_{*CO}) as a function of the overpotential ($\eta^{Charge} - \eta^{Disharge}$) on the above catalysts.

Information). In N-doped, S-doped, and N,S-codoped catalysts, it was found that the C atoms nearby the doped N heteroatom have a positive charge/spin density distribution and show high catalytic activity for CO_2 conversion (Figures S35 and S36, Supporting Information). For FeN_4 active centers, CO_2 conversion is more likely to occur at the Fe-sites because of their high positive charge. Among all the catalysts investigated in this study, the N-doped and S-doped catalysts have negligible spin density distribution on their skeleton, leading to poor catalytic conversion of CO_2. It is the synergistic effects between the charge and spin re-distribution induced by N,S-codoping (Figure S34, Supporting Information) and the presence of "Fe–N_4" moieties (Figure 5f) in the carbon skeleton that lead to the charge transfer between the carbon atoms and heteroatoms to effectively catalyze CO_2 reduction and evolution, and thus the high catalytic performance (Figure 5g).

As shown in Figure S37 (Supporting Information), there are three possible reaction pathways in Li–CO_2 conversion. Since the *COLi intermediate is thermodynamically unstable and does not form on the catalyst, the pathways II and III seem impossible. Herein, subsequent theoretical calculations focused on the pathway I (Figure S38, Supporting Information). Figures 5h,i show the free energy diagrams of discharge and charge, respectively, for FeN_4-containing, N- and/or S-doped catalysts. During the discharging process, the elementary reaction of *C formation is the rate-determining step for all the catalysts except FeN_4-edge with the sixth step of *$COCO_2Li$ intermediate formation as the rate-determining (Figure 5h). While for the reverse process of charging, the large energy barrier for the first step (Figure 5i) suggests that the elementary reaction of *C formation on the catalyst surface is the rate-determining step for all these catalysts. According to the free energy of these rate-determining step, we calculated the overpotential ($\eta^{discharging}$ and $\eta^{charging}$) for discharging and charging (Table S3, Supporting Information). The edge "FeN_4" moiety exhibits the lowest charging potential (4.06 V) in the charging process and the highest output potential (2.92 V) in the discharging process (Figure 5i and Table S3, Supporting Information), indicating the cell performance even better than that of the Fe single atoms anchored on an FeN_4-containing graphene plane with a 4.11 V charging potential and 2.87 V discharging potential (Figure 5j and Table S3, Supporting Information). According to the calculated potentials for charging and discharging and the corresponding overpotential values (Figure 5j and Table S3, Supporting Information), the catalytic activities are in the order of Fe-ISA/N,S-HG > N-doped HG > S-doped HG > HG, which is consistent with the experimental results. Specifically, the overpotentials for charging (4.06 V) and discharging (2.87 V) determined by the calculations are in good agreement with our experimental data (3.95 and 2.78 V for charging and discharging, respectively) for Fe-ISA/N,S-HG catalysts (Table S3, Supporting Information).

In summary, we have successfully implanted single iron atoms into N,S-codoped HG to produce the 3D porous Fe-ISA/N,S-HG catalysts, showing great potential for high-performance Li–CO_2 batteries. The resultant rechargeable Li–CO_2 batteries exhibited a low potential gap of ≈1.17 V at 100 mA g^{-1} while repeatedly charging and discharging for over 200 cycles with a cut-off capacity of 1000 mAh g^{-1} at a high current density of 1 A g^{-1}. The observed superior cycling stability and small polarization in the formation and decomposition of Li_2CO_3 during discharge/charge processes are attributable to their high catalytic activities. The high catalytic activity, combined with the lack of Fe atom aggregation during cycling, led to the formation of small dense Li_2CO_3 nanoparticles anchored over the Fe-ISA/N,S-HG catalyst, which could be readily decomposed during the charging process. Our DFT calculations correlated the observed appealing catalytic performance with the hierarchical structure of the carbon catalyst, revealing the synergistic effects between the charge and spin re-distribution induced by N,S-codoping and the presence of "Fe–N_4" moieties in the carbon skeleton to effectively catalyze CO_2 reduction and evolution. This work provides an effective approach to the design and development of new highly efficient catalytic cathodes for metal–CO_2 batteries and beyond.

Supporting Information

Supporting Information is available from the Wiley Online Library or from the author.

Acknowledgements

This work was partially supported by NASA (NNX16AD48A) and ARC (DP 190103881 and FL 190100126). The work at Argonne National Laboratory was also supported by the U.S. Department of Energy (DOE), Office of Energy Efficiency and Renewable Energy, Vehicle Technologies Office. Argonne National Laboratory is operated for DOE Office of Science by UChicago Argonne, LLC, under contract number DE-AC02-06CH11357. R.S.-Y. acknowledges the financial support from NSF-DMR Award No. 1809439. This work made use of instruments in the Electron Microscopy Service (Research Resources Center, UIC). This research used resources of the Advanced Photon Source (9-BM and 12-BM), a U.S. Department of Energy (DOE) Office of Science User Facility operated for the DOE Office of Science by Argonne National Laboratory under Contract No. DE-AC02-06CH11357. The authors thank Dr. Ben Reinhart for assistance with XAS experiments.

Conflict of Interest

The authors declare no conflict of interest.

Keywords

3D carbon, bifunctional catalysis, holey graphene, rechargeable Li–CO_2 batteries, single-atom catalysts

Received: November 12, 2019
Revised: January 20, 2020

---

[1] X. Duan, J. Xu, Z. Wei, J. Ma, S. Guo, S. Wang, H. Liu, S. Dou, *Adv. Mater.* **2017**, *29*, 1701784.
[2] C. Hu, Y. Lin, J. Connell, H.-M. Cheng, Y. Gogotsi, M.-M. Titirici, L. Dai, *Adv. Mater.* **2019**, *31*, 1806128.
[3] L. Qie, Y. Lin, J. Connell, J. Xu, L. Dai, *Angew. Chem., Int. Ed.* **2017**, *56*, 6970.
[4] W. Q. Ma, X. Z. Liu, C. Li, H. M. Yin, W. Xi, R. R. Liu, G. He, X. Zhao, J. Luo, Y. Ding, *Adv. Mater.* **2018**, *30*, 1801152.
[5] L. J. Wang, W. R. Dai, L. P. Ma, L. L. Gong, Z. Y. Lyu, Y. Zhou, J. Liu, M. Lin, M. Lai, Z. Q. Peng, W. Chen, *ACS Omega* **2017**, *2*, 9280.
[6] X. Li, S. X. Yang, N. N. Feng, P. He, H. S. Zhou, *Chin. J. Catal.* **2016**, *37*, 1016.
[7] Y. Xing, Y. Yang, D. H. Li, M. C. Luo, N. Chen, Y. S. Ye, J. Qian, L. Li, D. J. Yang, F. Wu, R. J. Chen, S. J. Guo, *Adv. Mater.* **2018**, *30*, 1803124.
[8] Y. Qiao, J. Yi, S. Wu, Y. Liu, S. Yang, P. He, H. Zhou, *Joule* **2017**, *1*, 359.
[9] S. X. Yang, Y. Qiao, P. He, Y. J. Liu, Z. Cheng, J.-J. Zhu, H. S. Zhou, *Energy Environ. Sci.* **2017**, *10*, 972.
[10] J. M. Chen, K. Y. Zou, P. Ding, J. Deng, C. Y. Zha, Y. P. Hu, X. Zhao, J. L. Wu, J. Fan, Y. G. Li, *Adv. Mater.* **2019**, *31*, 1805484.
[11] P. Tan, Z. H. Wei, W. Shyy, T. S. Zhao, X. B. Zhu, *Energy Environ. Sci.* **2016**, *9*, 1783.
[12] Z. Zhang, Q. Zhang, Y. A. Chen, J. Bao, X. L. Zhou, Z. J. Xie, J. P. Wei, Z. Zhou, *Angew. Chem., Int. Ed.* **2015**, *54*, 6550.
[13] X. Zhang, Q. Zhang, Z. Zhang, Y. N. Chen, Z. J. Xie, J. P. Wei, Z. Zhou, *Chem. Commun.* **2015**, *51*, 14636.
[14] Y. Jin, C. Hu, Q. Dai, Y. Xiao, Y. Lin, J. Connell, F. Chen, L. Dai, *Adv. Funct. Mater.* **2018**, *28*, 1804630.
[15] B. T. Qiao, A. Q. Wang, X. F. Yang, L. F. Allard, Z. Jiang, Y. T. Cui, J. Y. Liu, J. Li, T. Zhang, *Nat. Chem.* **2011**, *3*, 634.
[16] Y. J. Chen, S. F. Ji, Y. G. Wang, J. C. Dong, W. X. Chen, Z. Li, R. G. Shen, L. R. Zheng, Z. B. Zhuang, D. S. Wang, Y. D. Li, *Angew. Chem., Int. Ed.* **2017**, *56*, 6937.
[17] P. Z. Chen, T. P. Zhou, L. L. Xing, K. Xu, Y. Tong, H. Xie, L. D. Zhang, W. S. Yan, W. S. Chu, C. Z. Wu, Y. Xie, *Angew. Chem., Int. Ed.* **2017**, *56*, 610.
[18] H.-J. Qiu, Y. Ito, W. T. Cong, Y. W. Tan, P. Liu, A. Hirata, T. Fujita, Z. Tang, M. W. Chen, *Angew. Chem., Int. Ed.* **2015**, *54*, 14031.
[19] C. H. Zhang, S. Z. Yang, J. J. Wu, M. J. Liu, S. Yazdi, M. Q. Ren, J. W. Sha, J. Zhong, K. Q. Nie, A. S. Jalilov, Z. Y. Li, H. M. Li, B. I. Yakobson, Q. Wu, E. Ringe, H. Xu, P. M. Ajayan, J. M. Tour, *Adv. Energy Mater.* **2018**, *8*, 1703487.
[20] B.-W. Zhang, Y. Jiao, D.-L. C. C. Ye, Y.-X. Wang, K. Davey, H.-K. Liu, S.-X. Dou, S.-Z. Qiao, *Adv. Funct. Mater.* **2019**, *29*, 1904206.
[21] P. X. Liu, Y. Zhao, R. X. Qin, S. G. Mo, G. X. Chen, L. Gu, D. M. Chevrier, P. Zhang, Q. Guo, D. D. Zang, B. H. Wu, G. Fu, N. F. Zheng. *Science* **2016**, *52*, 797.
[22] H. L. Fei, J. C. Dong, M. J. Arellano-Jiménez, G. L. Ye, N. D. Kim, E. L. G. Samuel, Z. W. Peng, Z. Zhu, F. Qin, J. M. Bao, M. Jose Yacaman, P. M. Ajayan, D. L. Chen, J. M. Tour, *Nat. Commun.* **2015**, *6*, 8668.
[23] H. T. Sun, L. Mei, J. F. Liang, Z. P. Zhao, C. Lee, H. L. Fei, M. N. Ding, J. Lau, M. F. Li, C. Wang, X. Xu, G. L. Hao, *Science* **2017**, *356*, 599.

[24] D. H. Guo, R. K. Shibuya, C. Akiba, S. Saji, T. Kondo, J. Nakamura, *Science* **2016**, *351*, 361.
[25] H. G. Liang, Y. L. Zhang, F. Chen, S. Y. Jing, S. B. Yin, P. Tsiakaras, *Appl. Catal., B* **2019**, *244*, 559.
[26] C. Li, G. Shi, *Nanoscale* **2012**, *4*, 5549.
[27] U. I. Kramm, I. Herrmann, S. Fiechter, G. Zehl, I. Zizak, I. Abs-Wurmbach, J. Radnik, I. Dorbandt, P. Bogdanoff, *ECS Trans.* **2009**, *25*, 659.
[28] S. Lacey, D. Kirsch, Y. Li, J. Morgenstern, B. Zarket, Y. Yao, J. Dai, L. Garcia, B. Liu, T. Gao, S. Xu, S. Raghavan, J. Connell, Y. Lin, L. Hu, *Adv. Mater.* **2018**, *30*, 1705651.
[29] A. C. Ferrari, J. Robertson, *Phys. Rev. B* **2000**, *61*, 14095.
[30] P. Lespade, R. Al-Jishi, M. S. Dresselhaus, *Carbon* **1982**, *20*, 427.
[31] C. Hu, J. Xue, L. Dong, Y. Jiang, X. Wang, L. Qu, L. Dai, *ACS Nano* **2016**, *10*, 1325.
[32] M. A. Pimenta, G. Dresselhaus, M. S. Dresselhaus, L. G. Cançado, A. Jorio, R. Saito, *Phys. Chem. Chem. Phys.* **2007**, *9*, 1276.
[33] L. G. Cançado, A. Jorio, E. H. Martins Ferreira, F. Stavale, C. A. Achete, R. B. Capaz, M. V. O. Moutinho, A. Lombardo, T. S. Kulmala, A. C. Ferrari, *Nano Lett.* **2011**, *11*, 3190.
[34] C. Hu, L. Wang, Y. Zhao, M. Ye, Z. Feng, L. Qu, *Nanoscale* **2014**, *6*, 8002.
[35] Y. Zhao, C. Hu, Y. Hu, H. Cheng, G. Shi, L. Qu, *Angew. Chem., Int. Ed.* **2012**, *51*, 11371.
[36] Q. G. He, X. F. Yang, X. M. Ren, B. E. Koel, N. Ramaswamy, S. Mukerjeed, R. Kostecki, *J. Power Sources* **2011**, *196*, 7404.
[37] J. K. Li, S. Ghoshai, W. T. Liang, M.-T. Sougrati, F. Haouen, B. Halevi, S. Mckinney, G. McCool, C. R. Ma, X. X. Yuan, Z.-F. Ma, S. Mukerjee, Q. Y. Jia, *Energy Environ. Sci.* **2016**, *9*, 2418.
[38] W.-J. Jiang, L. Gu, L. Li, Y. Zhang, X. Zhang, L.-J. Zhang, J.-Q. Wang, J.-S. Hu, Z. Wei, L.-J. Wan, *J. Am. Chem. Soc.* **2016**, *138*, 3570.
[39] C. Hu, L. Lv, J. Xue, M. Ye, L. Wang, L. Qu, *Chem. Mater.* **2015**, *27*, 5253.
[40] C. Hu, L. Dai, *Adv. Mater.* **2017**, *29*, 1604942.
[41] A. Zitolo, V. Goellner, V. Armel, M.-T. Sougrati, T. Mineva, L. Stievano, E. Fonda, F. Jaouen, *Nat. Mater.* **2015**, *14*, 937.
[42] D. H. Deng, X. Q. Chen, L. Yu, X. Wu, Q. F. Liu, Y. Liu, H. X. Yang, H. F. Tian, Y. F. Hu, P. P. Du, R. Si, J. H. Wang, X. J. Cui, H. B. Li, J. P. Xiao, T. Xu, J. Deng, F. Yang, P. N. Duchesne, P. Zhang, J. G. Zhou, L. T. Sun, J. Q. Li, X. L. Pan, X. H. Bao, *Sci. Adv.* **2015**, *1*, e1500462.
[43] H. T. Chung, D. A. Cullen, D. Higgins, B. T. Sneed, E. F. Holby, K. L. More, P. Zelenay, *Science* **2017**, *357*, 479.
[44] K. Xia, F. Weesner, W. F. Bleam, P. R. Bloom, U. L. Skyllberg, P. A. Helmke, *Soil Sci. Soc. Am. J.* **1998**, *62*, 1240.
[45] Q. H. Li, W. X. Chen, H. Xiao, Y. Gong, Z. Li, L. R. Zheng, X. S. Zheng, W. S. Yan, W.-C. Cheong, R. A. Shen, N. H. Fu, L. Gu, Z. B. Zhuang, C. Chen, D. S. Wang, Q. Peng, J. Li, Y. D. Li, *Adv. Mater.* **2018**, *30*, 1800588.
[46] C. Hu, Y. Xiao, Y. Zou, L. Dai, *Electrochem. Energy Rev.* **2018**, *1*, 84.
[47] C. Hu, Y. Xiao, Y. Zhao, N. Chen, Z. Zhang, M. Cao, L. Qu, *Nanoscale* **2013**, *5*, 2726.
[48] F. Qiu, S. Ren, X. Mu, Y. Liu, X. Zhang, P. He, H. Zhou, *Energy Storage Mater.* **2020**, *26*, 443.
[49] X. Zhang, Q. M. Zhang, X.-G. Wang, C. Y. Wang, Y.-N. Chen, Z. J. Xie, Z. Zhou, *Angew. Chem., Int. Ed.* **2018**, *130*, 1299.
[50] M. H. Bai, K. Y. Xie, K. Yuan, K. Zhang, N. Li, C. Shen, Y. Q. Lai, R. Vajtai, P. Ajayan, B. Wei, *Adv. Mater.* **2018**, *30*, 1801213.
[51] C. Z. Shu, Y. M. Lin, D. S. Su, *J. Mater. Chem. A* **2016**, *4*, 2128.
[52] G. Kresse, J. Furthmüller, *Comput. Mater. Sci.* **1996**, *6*, 15.
[53] G.-L. Chai, Z.-X. Guo, *Chem. Sci.* **2016**, *7*, 1268.